

Electronic structure and carrier mobility of BSb nanotubes

Lantian Xue(薛岚天), Chennan Song(宋晨楠), Miaomiao Jian(见苗苗), Qiang Xu(许强), Yuhao Fu(付钰豪), Pengyue Gao(高朋越), and Yu Xie(谢禹)

Citation: Chin. Phys. B, 2025, 34 (**3**): 037304. DOI: 10.1088/1674-1056/adacd3
Journal homepage: http://cpb.iphy.ac.cn; http://iopscience.iop.org/cpb

What follows is a list of articles you may be interested in

Facile fabrication of highly flexible, porous PEDOT: PSS/SWCNTs films for thermoelectric applications

Fu-Wei Liu(刘福伟), Fei Zhong(钟飞), Shi-Chao Wang(王世超), Wen-He Xie(谢文合), Xue Chen(陈雪), Ya-Ge Hu(胡亚歌), Yu-Ying Ge(葛钰莹), Yuan Gao(郜源), Lei Wang(王雷), and Zi-Qi Liang(梁子骐)
Chin. Phys. B, 2022, 31 (**2**): 027303. DOI: 10.1088/1674-1056/ac3502

Electronic and magnetic properties of CrI_3 nanoribbons and nanotubes

Ji-Zhang Wang(王吉章), Jian-Qi Huang(黄建啟), Ya-Ning Wang(王雅宁), Teng Yang(杨腾), Zhi-Dong Zhang(张志东)
Chin. Phys. B, 2019, 28 (**7**): 077301. DOI: 10.1088/1674-1056/28/7/077301

Electronic transport properties of single-wall boron nanotubes

Xinyue Dai(代新月), Yi Zhou(周毅), Jie Li(李洁), Lishu Zhang(张力舒), Zhenyang Zhao(赵珍阳), Hui Li(李辉)
Chin. Phys. B, 2017, 26 (**8**): 087310. DOI: 10.1088/1674-1056/26/8/087310

Advantages of using gold hollow nanoshells in cancer photothermal therapy

Sattar Abbasi, Mojtaba Servatkhah, Mohammad Mehdi Keshtkar
Chin. Phys. B, 2016, 25 (**8**): 087301. DOI: 10.1088/1674-1056/25/8/087301

Vibration and buckling analyses of nanobeams embedded in an elastic medium

S Chakraverty, Laxmi Behera
Chin. Phys. B, 2015, 24 (**9**): 097305. DOI: 10.1088/1674-1056/24/9/097305

RAPID COMMUNICATION

Electronic structure and carrier mobility of BSb nanotubes

Lantian Xue(薛岚天)[1,2], Chennan Song(宋晨楠)[2], Miaomiao Jian(见苗苗)[1,2,†], Qiang Xu(许强)[2,‡], Yuhao Fu(付钰豪)[1,2], Pengyue Gao(高朋越)[2,§], and Yu Xie(谢禹)[2,3]

[1] *State Key Laboratory of High Pressure and Superhard Materials, College of Physics, Jilin University, Changchun* 130012, *China*
[2] *Key Laboratory of Material Simulation Methods & Software of Ministry of Education, College of Physics, Jilin University, Changchun* 130012, *China*
[3] *Key Laboratory of Physics and Technology for Advanced Batteries of Ministry of Education, College of Physics, Jilin University, Changchun* 130012, *China*

(Received 31 December 2024; revised manuscript received 20 January 2025; accepted manuscript online 22 January 2025)

High-mobility semiconductor nanotubes have demonstrated great potential for applications in high-speed transistors, single-charge detection, and memory devices. Here we systematically investigated the electronic properties of single-walled boron antimonide (BSb) nanotubes using first-principles calculations. We observed that rolling the hexagonal boron antimonide monolayer into armchair (ANT) and zigzag (ZNT) nanotubes induces compression and wrinkling effects, significantly modifying the band structures and carrier mobilities through band folding and π^*–σ^* hybridization. As the chiral index increases, the band gap and carrier mobility of ANTs decrease monotonically, where electron mobility consistently exceeds hole mobility. In contrast, ZNTs exhibit a more complex trend: the band gap first increases and then decreases, and the carrier mobility displays oscillatory behavior. In particular, both ANTs and ZNTs could exhibit significantly higher carrier mobilities compared to hexagonal monolayer and zinc-blende BSb, reaching 10^3–10^7 cm^2·V^{-1}·s^{-1}. Our findings highlight strong curvature-induced modifications in the electronic properties of single-walled BSb nanotubes, demonstrating the latter as a promising candidate for high-performance electronic devices.

Keywords: *ab initio* calculations, nanotubes, electronic structure, carrier mobility

PACS: 73.63.Fg, 61.46.Fg, 51.50.+v, 91.60.Tn

DOI: 10.1088/1674-1056/adacd3 **CSTR:** 32038.14.CPB.adacd3

1. Introduction

Low-dimensional materials have attracted much attention for their unique properties and promising applications in next-generation electronic devices.[1–5] An important example is the experimental exfoliation of single-layer graphene, which has attracted enormous attention for its exceptional intrinsic carrier mobility.[6,7] However, graphene's zero-bandgap semi-metallic nature restricts its applications in electronic devices.[8] Therefore, identifying materials with a balanced combination of moderate band gap and high carrier mobility has gradually become a central focus in low-dimensional materials to address the limitation of graphene and unlock new opportunities for advanced technologies.[9–11]

Two-dimensional (2D) III–V compounds, especially the compounds between boron and V group (BN, BP, BAs, and BSb), have drawn significant attention for their narrow direct band gap, low ionicity, high thermal conductivity, and high melting point, making them promising materials for applications in optoelectronic devices and high-temperature environments.[12–38] Recent studies have shown that BP, BAs, and BSb monolayers exhibit extremely high carrier mobilities, where the reported hole and electron carrier mobilities are generally above 10^3 cm^2·V^{-1}·s^{-1},[39,40] indicating that these B–V compounds are promising for high-performance electronic devices.[26,41] Notably, rolling up 2D materials to form one-dimensional (1D) nanotubes (NT) could further tune the electronic properties of the materials, which may lead to the presentation of unique properties.[42–44] Indeed, several previous works reported that the BP and BAs NTs show higher carrier mobilities than their 2D counterparts, reaching up to 10^4 cm^2·V^{-1}·s^{-1} and 10^5 cm^2·V^{-1}·s^{-1}, respectively.[45,46] This confirms that reducing the dimensionality to introduce strong confinements is a useful way to enhance the transportation of carriers in materials. Given that BSb monolayer exhibits the highest carrier mobilities among 2D B–V semiconductors, surpassing 5×10^3 cm^2·V^{-1}·s^{-1},[39,40] it is intriguing to explore the electronic properties of BSb nanotubes to examine whether they can achieve even higher carrier mobilities.

In this work, we employed first-principles method to investigate the electronic properties and carrier mobilities of single-walled 1D armchair BSb NTs (ANTs) with chiral index (n, n) for $n = 5$ to 14 and zigzag BSb NTs (ZNTs) with chiral index (n, 0) for $n = 5$ to 22. Similar band structures to those of C, BN, and BAs were observed, with the direct band gaps of ANTs and ZNTs converging to the planar counter-

†Corresponding author. E-mail: mmjian424@gmail.com
‡Corresponding author. E-mail: xq@calypso.cn
§Corresponding author. E-mail: gpy@calypso.cn

© 2025 Chinese Physical Society and IOP Publishing Ltd. All rights, including for text and data mining, AI training, and similar technologies, are reserved.

parts. The carrier mobilities of ANTs and ZNTs were assessed using the Boltzmann transport equation within the relaxation-time approximation. The estimated mobility is higher than the monolayer counterpart and ranges from 10^3 $cm^2{\cdot}V^{-1}{\cdot}s^{-1}$ to 10^7 $cm^2{\cdot}V^{-1}{\cdot}s^{-1}$, highlighting the potential of 1D BSb NTs for advanced electronic devices applications.

2. Computational methodology

All calculations were performed using Quantum ESPRESSO[47,48] and verified with *Ab initio* Real-space Electronic Structure (ARES) code,[49,50] employing Perdew–Burke–Ernzerhof (PBE) exchange–correlation functional.[51] The norm-conserving pseudopotentials generated by optimized norm-conserving Vanderbilt (ONCV) pseudopotential code[52] were adopted for all geometry optimization and electronic properties simulations. The energy cutoff of 80 Ry was used for all calculations, and the maximum force was converged to 10^{-4} Ry/Bohr for all geometry optimizations. For the planar h-BSb, a 30 Å vacuum layer was introduced to eliminate electrostatic interactions between periodic images, along with $24\times24\times1$ k-point meshes for accurate sampling.[53] For BSb NTs, we designed single-walled ANTs and ZNTs based on the chiral indices (n,n) and $(n,0)$, respectively.[54,55] As illustrated in Fig. 1, ANTs and ZNTs display varying periodic unit lengths along the tube axis (z axis) and distinct radii determined by the chiral index n. Specifically, for ANTs, the periodic unit has an initial length of a along the axial direction and $\sqrt{3}a$ in the circumferential direction; whereas for ZNTs, the initial periodic unit length is $\sqrt{3}a$ in the axial direction and a in the circumferential direction. Here, a denotes the lattice constant of the primitive cell of the BSb monolayer. The k-point grid meshes were set to $1\times1\times24$ for ANTs and $1\times1\times14$ for ZNTs. A sufficient vacuum distance of 20 Å was applied in the non-periodic directions for all NTs. Additionally, convergence tests for energy cutoffs and k-point sampling are shown in Fig. S1.[56]

To investigate the transport behavior of BSb NTs, the Boltzmann transport equation with relaxation-time approximation was employed to study the carrier mobility. To model the scattering process, accounting solely for the coupling between electrons and long-wavelength acoustic phonons, the deformation potential (DP) method[57] was used in conjunction with the effective mass approximation. The 1D mobility is given by[58]

$$\mu = \frac{e\tau}{m^*} = \sqrt{\frac{2}{\pi}}\frac{e\hbar^2 C}{(k_{\mathrm{B}}T)^{1/2}|m^*|^{3/2}E_{\mathrm{D}}^2}, \tag{1}$$

where τ is the scattering relaxation time, m^* is the effective mass, E_{D} is the DP constant for hole or electron, and C is the elastic constant. These parameters are obtained as follows:

$$\frac{1}{m^*} = \frac{1}{\hbar^2}\left(\frac{\partial^2\varepsilon(\boldsymbol{k})}{\partial\boldsymbol{k}^2}\right), \tag{2}$$

$$E_{\mathrm{D}} = \frac{\varepsilon_{\mathrm{M}}}{\left(\frac{\Delta L}{L_0}\right)}, \tag{3}$$

$$C = \frac{1}{L_0}\frac{\partial^2 E}{\partial\left(\frac{\Delta L}{L_0}\right)^2}, \tag{4}$$

where $\varepsilon(\boldsymbol{k})$ is the band energy as a function of k points, ε_{M} denotes the energy of valence band maximum (VBM) or conduction band minimum (CBM) referenced to the vacuum energy, L_0 is the lattice constant in the unstrained state, and $\Delta L/L_0$ denotes the uniaxial strain. So far, the mobility of holes (μ_{h}) or electrons (μ_{e}) for BSb NTs at different temperatures can be obtained by applying various deformations along the tube direction. In this work, we applied 11 deformations of the lattice constant ranging from $-0.010L_0$ to $0.010L_0$ with an interval of $0.002L_0$. The least squares method was employed to fit C and E_{D} using first-order and second-order polynomials, respectively. The fitting results and root mean square errors of ANTs are shown in Figs. S2 and S3, respectively, while those of ZNTs are shown in Figs. S4 and S5, respectively.[56]

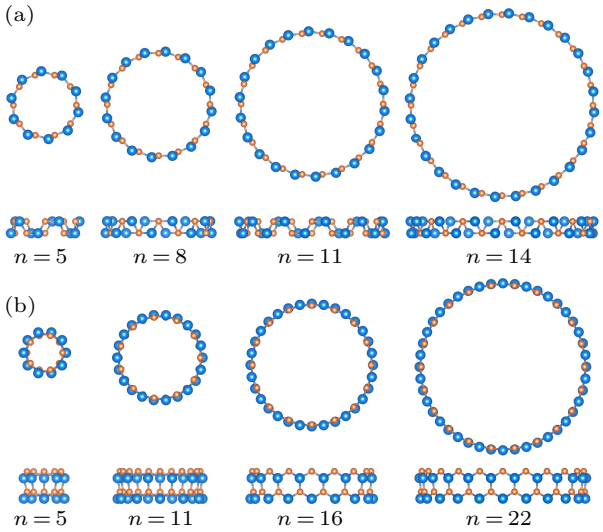


Fig. 1. Structures of BSb nanotubes with varying chiral indices n. Blue and orange spheres represent Sb and B atoms, respectively. (a) Armchair-direction nanotubes and (b) zigzag-direction nanotubes, shown in top and side views.

3. Results and discussion

Before investigating NTs, we first calculated the electronic structure properties of monolayer h-BSb to facilitate comparison between planar and NTs. As shown in Fig. 2, geometry optimization and band structure calculations reveal a B–Sb bond length of 2.15 Å and a direct band gap of 0.31 eV at K point, both of which agree well with previously reported values.[21,35]

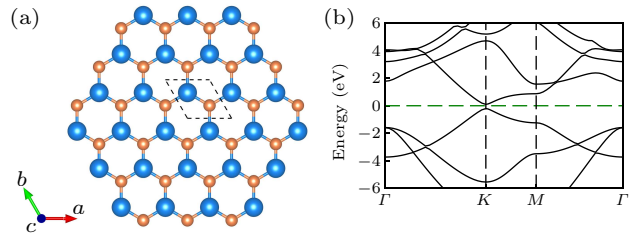


Fig. 2. (a) Optimized structure of the monolayer h-BSb, where blue and orange spheres represent Sb and B atoms, respectively. The dashed rhombus indicates the unit cell. (b) The band structure of h-BSb with a direct band gap at the K point.

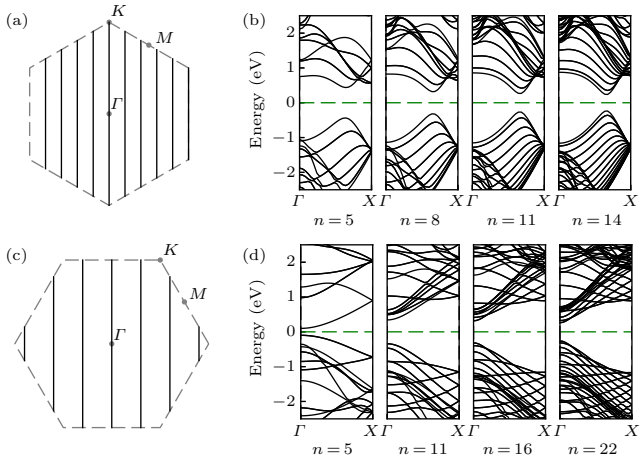


Fig. 3. The Brillouin zone and band structures of BSb nanotubes: [(a) and (c)] The first Brillouin zone of a hexagonal BSb sheet (dashed line), along with the allowed wave vectors (solid lines) for ANT and ZNT at chiral indices $n = 5$, respectively. The wave vectors are constrained by the periodic boundary conditions along the circumference direction. [(b) and (d)] Band structures of ANTs and ZNTs with varying chiral indices n (from left to right: $n = 5, 8, 11, 14$ for ANT and $n = 5, 11, 16, 22$ for ZNT). The green dashed line indicates the Fermi level.

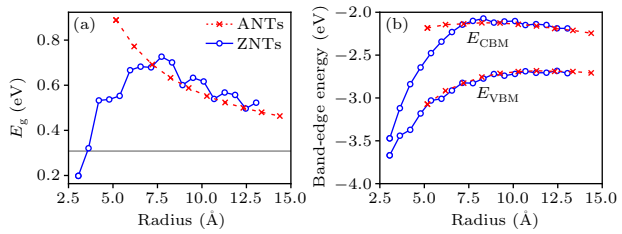


Fig. 4. (a) Band gap (E_g) as a function of the nanotube radius for ZNTs and ANTs. The gray line indicates the band gap of the monolayer h-BSb. (b) The corresponding band-edge energies (E_{VBM} and E_{CBM}) of ANTs and ZNTs.

As shown in Fig. 3, similar behaviors to those observed in C, BN, and BAs NTs[46,59–61] were also found in BSb NTs. Specifically, ANTs exhibit a slightly larger direct band gap compared to planar h-BSb around the 2/3 point along the Γ–X k-path. In contrast, ZNTs display direct band gaps that initially increase and then decrease at the Γ point with increasing chiral index n. To understand the mechanism behind the band gap variation, the relationship between the band gaps and the radii of the NTs is presented in Fig. 4(a). For ZNTs with small radii (< 3.0 Å), strong π^*–σ^* hybridization occurs, lowering the energy of the π^* states and resulting in a relatively small band gap compared to that of planar h-BSb. As the radius increases, the effects of π^*–σ^* hybridization gradually weaken, and the band gap begins to exhibit behavior similar to that of ANTs, decreasing monotonically with increasing radius. Furthermore, the k vectors allowed by the periodic boundary condition along the circumferential direction do not always pass through the K point in h-BSb, as shown in Fig. 3(c). After folding the allowed k-vectors in the Brillouin zone of ZNTs, this results in the alternating $3p$ fluctuation pattern observed in the band gaps of ZNTs, with p being an integer.[59] A more direct comparison of the band gap behavior between ZNTs and ANTs is shown in Fig. 4(b). The energies of the VBM and CBM are presented relative to the vacuum energy to align the energy levels across different systems. For ZNTs, the E_{CBM}, dominated by the π^* states,[60] is significantly influenced by hybridization effects when the radius is small, leading to a notable shift in energy. As the radius increases, these hybridization effects gradually diminish, and the band energies gradually approach those of ANTs, where both the E_{VBM} and E_{CBM} primarily originate from the band folding of the 2D h-BSb monolayer. In summary, although the band gaps of BSb NTs decrease slightly with increasing chiral index n, the curvature-induced enhancement of the band gap suggests potential for optical applications.

The rolling effect is clearly evident in the structural characteristics shown in Figs. 5(a)–5(c). The BSb NTs are compressed along the tube axis, and the lattice dilation increases with the chiral index, eventually approaching the ideal lattice constant without compression. Along the circumference, the B and Sb atoms are distorted, with B atoms positioned on the inner tube wall and Sb atoms on the outer tube wall. The distance between the two walls decreases as the chiral index increases. Moreover, the distortion in ANTs is more significant than that in ZNTs, even when they have similar radii. For example, ANT(8,8) shows greater distortion compared to ZNT(14,0). Further analysis was carried out to explore the curling energy of BSb NTs. For a BSb NT with chiral index n, the unit cell contains $2n$ primitive cells of h-BSb. Therefore, the curling energy per formula unit of BSb NTs is given by

$$E_{curl} = E_{tube}/(2n) - E_{h-BSb}. \tag{5}$$

As shown in Fig. 5(d), the curling energy per formula is smaller than 50 meV when the radius is around 5 Å, which is significantly lower than that of BN and carbon nanotubes[61,62] and close to the value for BAs,[46] indicating a strong buckling effect that reduces the energy of BSb NTs, making it more favorable to fold a h-BSb sheet into a nanotube compared to BN or carbon.

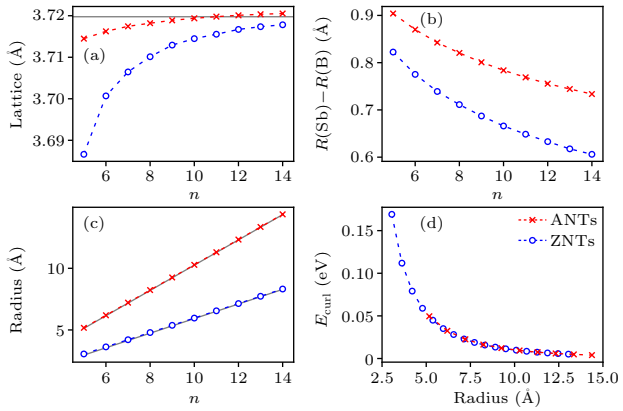


Fig. 5. Structural and energetic properties of ZNTs and ANTs with different chiralities. (a) The variation of the optimized lattice constant with respect to the chiral indices n, where the lattice constant of ZNTs is normalized for comparison by the factor $\sqrt{3}/3$. (b) The variation in the optimized diameter difference between B and Sb atoms, caused by wrinkling of the nanotube wall, with respect to the chiral indices n. (c) The radius of the nanotube corresponding to different chiral indices n. (d) Curling energy per formula as a function of the radius of BSb nanotubes with respect to the energy of h-BSb. The gray lines in panels (a) and (c) represent the non-optimized values calculated from the h-BSb monolayer.

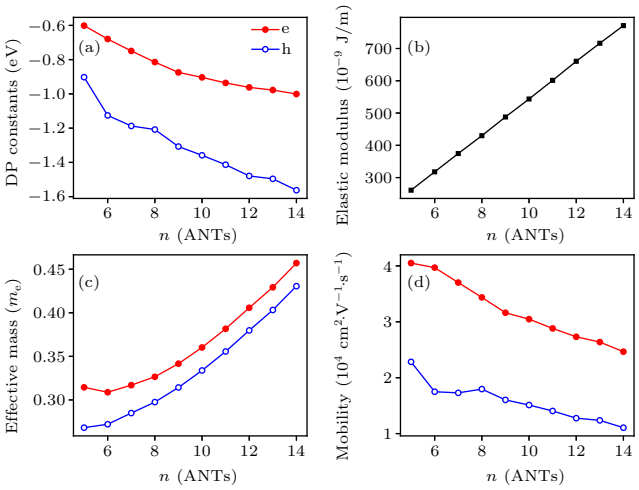


Fig. 6. Carrier transport properties of ANTs as a function of the chiral index n. (a) Deformation potential constants for electrons (e) and holes (h). (b) Elastic modulus. (c) Effective masses of electrons and holes, in units of the free electron mass (m_e). (d) Carrier mobilities of electrons and holes.

To further investigate the potential applications of BSb NTs in electronic devices, the carrier mobility at room temperature (300 K) was calculated. For ANTs, as shown in Fig. 6, the DP constants (E_D), obtained using Eq. (3), exhibit a monotonic decrease with increasing chiral index n for both electrons and holes. The increasing absolute values of E_D indicate stronger acoustic phonon scattering, which leads to reduced carrier mobilities. According to Eq. (1), the mobility μ is positively correlated with the elastic modulus and negatively correlated with the effective mass (m^*) and $|E_D|$. Although both the elastic modulus and effective mass increase nearly linearly with n, the dominant influence of the rising $|E_D|$ causes the mobilities of electrons (μ_e) and holes (μ_h) to decrease with increasing n. At $n = 14$, corresponding to an ANT with radius of 14.4 Å, the mobilities reach their lowest values among the calculated ANTs, with μ_e of 1.9×10^4 cm^2·V^{-1}·s^{-1} and μ_h of 4.3×10^4 cm^2·V^{-1}·s^{-1}.

For ZNTs (shown in Fig. 7), the elastic constants increase linearly with n, exhibiting a trend similar to that observed in ANTs. The $|E_D|$ and m^* show comparable behavior, consistent with findings in BAs nanotubes.[46] Specifically, the E_D of holes exhibits a $3p$-alternating behavior, while the E_D of electrons increases with n. However, for $n > 12$, the E_D of electrons transitions to a $3p$-alternating trend opposite to that of holes. This behavior could be attributed to the combined effects of π^*–σ^* hybridization[60] and band folding[59] in the h-BSb monolayer. The hybridization effect dominates for $n \leq 12$, leading to a decrease in $|E_D|$, while the band folding introduces distinct bonding behaviors[46] that give rise to the $3p$-alternating pattern. The carrier mobilities of ZNTs are primarily influenced by E_D and m^*. For $n = 5$, the mobilities are relatively small ($\mu_e = 1377$ cm^2·V^{-1}·s^{-1}, $\mu_h = 848$ cm^2·V^{-1}·s^{-1}) due to significant acoustic phonon scattering. As n increases, the E_D of holes fluctuates around zero, causing the μ_h to oscillate between 10^4 cm^2·V^{-1}·s^{-1} and 10^7 cm^2·V^{-1}·s^{-1}. This oscillatory behavior results from the disappearance of the $3p$-alternating trend in E_D^2. Meanwhile, the E_D of electrons decreases slowly, passing through zero for $n \leq 12$, leading to a large electron mobility ($\mu_e \approx 10^6$ cm^2·V^{-1}·s^{-1}). Beyond $n = 12$, the E_D of electrons begins exhibiting a $3p$-alternating behavior below zero, resulting in a corresponding oscillatory pattern in μ_e.

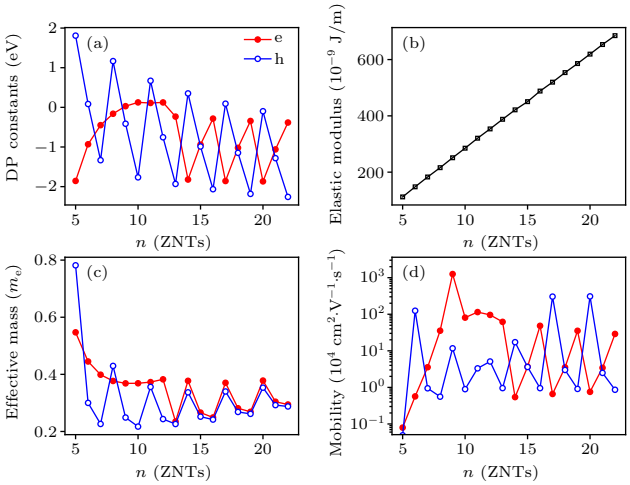


Fig. 7. Carrier transport properties of ZNTs as a function of the chiral index n. (a) Deformation potential constants for electrons (e) and holes (h). (b) Elastic modulus. (c) Effective mass for electrons and holes, in units of the free electron mass (m_e). (d) Carrier mobility for electrons and holes.

Overall, the calculated results demonstrate that the rolling process serves as an effective method for tuning the carrier transport properties of BSb structures. By rolling the h-BSb monolayer into armchair (ANTs) and zigzag nanotubes (ZNTs), compressive strain and wrinkling are introduced in different directions. A strong buckling effect is observed in

these nanotubes, facilitating their structural stability and ease of formation. The combined effects of band folding and π^*–σ^* hybridization lead to distinct behaviors in the electronic properties of ANTs and ZNTs. For ANTs, both the band gap and carrier mobilities decrease monotonically with increasing chiral index, yet the mobilities remain significant (μ_e of 1.9×10^4 cm^2·V^{-1}·s^{-1} and μ_h of 4.3×10^4 cm^2·V^{-1}·s^{-1}) for $n=14$. In contrast, ZNTs exhibit a more complex trend: the band gaps first increase and then decrease, while the carrier mobilities initially rise sharply and later display oscillatory behavior, spanning a wide range from 10^3 cm^2·V^{-1}·s^{-1} to 10^7 cm^2·V^{-1}·s^{-1} for both μ_e and μ_h.

4. Conclusion

In this work, first-principles calculations were employed to investigate the electronic properties of BSb NTs. The results reveal that band folding of the BSb monolayer and π^*–σ^* hybridization give rise to distinct band structures and carrier mobilities in ANTs and ZNTs. In ANTs, μ_e is consistently higher than μ_h, which both decrease as the radius increases. In contrast, ZNTs exhibit oscillatory mobilities, which can surpass those of ANTs in most cases. Notably, both types of BSb NTs demonstrate significantly higher carrier mobilities compared to the h-BSb monolayer or zinc-blende BSb bulk, underscoring their value for experimental validation and practical applications in electronic devices.

Acknowledgments

Project supported by the National Key R&D Program of China (Grant Nos. 2022YFA1402503, 2023YFA1406200, and 2023YFB3003001), the National Natural Science Foundation of China (Grant Nos. 12074138 and 12047530), the Interdisciplinary Integration and Innovation Project of JLU, Fundamental Research Funds for the Central Universities, and the Program for JLU Science and Technology Innovative Research Team (JLUSTIRT).

References

[1] Fan S, Feng X, Han Y, Fan Z and Lu Y 2019 *Nanoscale Horizons* **4** 781
[2] Fang J, Zhou Z, Xiao M, Lou Z, Wei Z and Shen G 2020 *InfoMat* **2** 291
[3] Ahmad W, Gong Y, Abbas G, Khan K, Khan M, Ali G, Shuja A, Tareen A K, Khan Q and Li D 2021 *Nanoscale* **13** 5162
[4] Liu Y, Duan X, Shin H J, Park S, Huang Y and Duan X 2021 *Nature* **591** 43
[5] Fu X, Liu Z, Wang H, Xie D and Sun Y 2024 *Advanced Science* **11** 2400500
[6] Novoselov K S, Geim A K, Morozov S V, Jiang D E, Zhang Y, Dubonos S V, Grigorieva I V and Firsov A A 2004 *Science* **306** 666
[7] Butler S Z, Hollen S M, Cao L, Cui Y, Gupta J A, Gutiérrez H R, Heinz T F, Hong S S, Huang J, Ismach A F, *et al.* 2013 *ACS Nano* **7** 2898
[8] Appelhans D J, Lin Z and Lusk M T 2010 *Phys. Rev. B* **82** 073410
[9] Biswas C and Lee Y H 2011 *Advanced Functional Materials* **21** 3806
[10] Ulian G and Valdrè G 2023 *Scientific Reports* **13** 23090
[11] Yao H, Guo X, Bao A, Mao H, Ma Y and Li X 2022 *Chin. Phys. B* **31** 038501
[12] Şahin H, Cahangirov S, Topsakal M, Bekaroglu E, Akturk E, Senger R T and Ciraci S 2009 *Phys. Rev. B* **80** 155453
[13] Topsakal M, Aktürk E and Ciraci S 2009 *Phys. Rev. B* **79** 115442
[14] Del Alamo J A 2011 *Nature* **479** 317
[15] Sarkar K, Devi P, Kim K H and Kumar P 2020 *TrAC Trends in Analytical Chemistry* **130** 115989
[16] Zhang S, Liu J, Kirchner M M, Wang H, Ren Y and Lei W 2021 *J. Phys. D: Appl. Phys.* **54** 433001
[17] Hossain N, Mobarak M H, Mimona M A, Islam M A, Hossain A, Zohura F T and Chowdhury M A 2023 *Results in Engineering* **19** 101347
[18] Golikova O 1979 *Phys. Status Solidi A Appl. Research* **51** 11
[19] Zaoui A and Hassan F E H 2001 *J. Phys.: Condens. Matter* **13** 253
[20] Pakdel A, Zhi C, Bando Y and Golberg D 2012 *Materials Today* **15** 256
[21] Zhuang H L and Hennig R G 2012 *Appl. Phys. Lett.* **101** 153109
[22] Lindsay L, Broido D and Reinecke T 2013 *Phys. Rev. Lett.* **111** 025901
[23] Yao Y, König D and Green M 2013 *Solar Energy Materials and Solar Cells* **111** 123
[24] Broido D, Lindsay L and Reinecke T 2013 *Phys. Rev. B* **88** 214303
[25] Ustundag M, Aslan M and Yalcin B G 2014 *Computational Materials Science* **81** 471
[26] Shi J, Han C, Wang X and Yun S 2019 *Physica B* **574** 311634
[27] Singh S, Gupta S K, Sonvane Y and Gajjar P 2018 *Phys. Lett. A* **382** 2978
[28] Manoharan K and Subramanian V 2018 *ACS Omega* **3** 9533
[29] Abderrahmane Y S, Menad A, Boutaiba F, Benyahia N, Zaoui A and Ferhat M 2021 *Materials Science in Semiconductor Processing* **136** 106138
[30] Matos E B 2024 *Mechanical Behaviour of Non-Carbon Nanotubes: a Numerical simulation study* Master's thesis
[31] Das S, Bhunia R, Hussain S, Bhar R, Chakraborty B and Pal A 2015 *Applied Surface Science* **353** 439
[32] Mishra P, Singh D, Sonvane Y and Gupta S K 2019 *AIP Conference Proceedings* **2142** 110019
[33] Tiwari V, Mal I, Agnihotri S K and Samajdar D P 2021 *Materials Science in Semiconductor Processing* **122** 105505
[34] Islam M R, Islam A J, Liu K, Wang Z, Qu S and Wang Z 2021 *Chemical Physics* **551** 111334
[35] Ersan F, Gökoğlu G and Aktürk E 2014 *J. Phys.: Condens. Matter* **26** 325303
[36] Al-Shammari A S I, Nia B A and Rezaee S 2024 *Physica Scripta* **99** 065970
[37] Ouyang X F and Wang L 2022 *Chin. Phys. B* **31** 077304
[38] Zhu X, Meng B, Wang D, Chen X, Liao L, Jiang M and Wei Z 2022 *Chin. Phys. B* **31** 047801
[39] Zhang C, Wang R, Mishra H and Liu Y 2023 *Phys. Rev. Lett.* **130** 087001
[40] Song S, Sun Y, Liu S, Yang J H and Gong X G 2023 *Phys. Rev. B* **107** 155101
[41] Kwon H J, Jang J and Grigoropoulos C P 2016 *ACS Applied Materials Interfaces* **8** 9314
[42] Xiao J, Long M, Li X, Xu H, Huang H and Gao Y 2014 *Scientific Reports* **4** 4327
[43] Zhang L, Hao Q, Liu J, Zhou J, Zhang W and Li Y 2022 *Chemical Engineering Journal* **446** 136937
[44] Aftab S, Iqbal M Z and Rim Y S 2023 *Small* **19** 2205418
[45] Li Q, Wang H, Yang C, Li Q and Rao W 2018 *Applied Surface Science* **441** 1079
[46] Dong Y, Zeng B, Zhang X, Li M, He J and Long M 2019 *J. Appl. Phys.* **126** 124303
[47] Giannozzi P, Baroni S, Bonini N, *et al.* 2009 *J. Phys.: Condens. Matter* **21** 395502
[48] Giannozzi P, Andreussi O, Brumme T, *et al.* 2017 *J. Phys.: Condens. Matter* **29** 465901
[49] Xu Q, Wang S, Xue L, Shao X, Gao P, Lv J, Wang Y and Ma Y 2019 *J. Phys.: Condens. Matter* **31** 455901
[50] Xue L, Xu Q, Ma C, Mi W, Wang Y, Xie Y and Ma Y 2024 *Phys. Rev. B* **110** 155157
[51] Perdew J P, Burke K and Ernzerhof M 1996 *Phys. Rev. Lett.* **77** 3865

[52] Hamann D 2013 *Phys. Rev. B* **88** 085117
[53] Monkhorst H J and Pack J D 1976 *Phys. Rev. B* **13** 5188
[54] Saito R, Fujita M, Dresselhaus G and Dresselhaus M 1992 *Appl. Phys. Lett.* **60** 2204
[55] Mintmire J and White C 1998 *Phys. Rev. Lett.* **81** 2506
[56] See supplemental material for detailed fitting informations of elastic constant and deformation potential constant; convergence tests of energy cutoff and *k*-points for both armchair nanotubes and zigzag nanotubes.
[57] Bardeen J and Shockley W 1950 *Phys. Rev.* **80** 72
[58] Beleznay F, Bogár F and Ladik J 2003 *The Journal of Chemical Physics* **119** 5690
[59] Hamada N, Sawada S i and Oshiyama A 1992 *Phys. Rev. Lett.* **68** 1579
[60] Blase X, Benedict L X, Shirley E L and Louie S G 1994 *Phys. Rev. Lett.* **72** 1878
[61] Xiang H, Yang J, Hou J and Zhu Q 2003 *Phys. Rev. B* **68** 035427
[62] Blase X, Rubio A, Louie S G and Cohen M L 1994 *Europhys. Lett.* **28** 335